FUSION SCIENCE AND TECHNOLOGY · VOLUME 75 · 283–298 · MAY 2019

DOI: https://doi.org/10.1080/15361055.2019.1565481

Discrete Element Analysis of Heat Transfer in the Breeder Beds of the European Solid Breeder Blanket Concept

M. Moscardini,[a]* S. Pupeschi,[a] Y. Gan,[b] F. A. Hernández,[c] and M. Kamlah[a]

[a]*Karlsruhe Institute of Technology, Institute for Applied Materials, Karlsruhe, Germany*
[b]*The University of Sydney, School of Civil Engineering, Sydney, NSW 2006, Australia*
[c]*Karlsruhe Institute of Technology, Institute for Neutron Physics and Reactor Technology, Karlsruhe, Germany*

Received September 13, 2018
Accepted for Publication January 3, 2019

Abstract — *In this work, an in-house thermal–Discrete Element Method (DEM) code, recently developed at Karlsruhe Institute of Technology to evaluate the heat transfer in ceramic packed pebble beds, was applied to study the thermal behavior of the breeder beds of the European solid breeder blanket concept. The breeder zone of the helium-cooled pebble bed (HCPB) blanket for the Demonstration (DEMO) reactor was considered as the reference model implementing the same materials, applying the related neutronic heating, and simulating the relevant bed thicknesses. The code was used to evaluate the temperature profile generated by the neutronic heating in the thickness of the breeder bed. A column cutout of packed pebbles bounded by upper and bottom walls, representing the cooling plates of the HCPB, was considered as a representative geometry to carry out the work. The implemented three-dimensional network model evaluates the heat transfer inside packed beds through chains of thermal resistances describing the thermal contacts (particle-particle and particle-wall) occurring in the assembly. Besides thermal transport through the mechanical contact area, thermal transport through the surrounding gas phase is accounted for including the Smoluchowski effect. Sensitivity studies revealed the influence of the operational conditions and the parameters that mainly affect the temperature profile in the bed.*

Keywords — *Discrete Element Method, thermal-DEM code, helium-cooled pebble bed.*

Note — *Some figures may be in color only in the electronic version.*

I. INTRODUCTION

For the self-sustainment of the tritium fuel in a nuclear fusion reactor, a tritium breeder and a neutron multiplier material are required. Both materials are located in the breeder blanket, a compulsory component for the future Demonstration (DEMO) power reactor.[1] Different breeder blanket concepts will be tested in the International Thermonuclear Experimental Reactor (ITER), the step before DEMO, to show that operating targets can be achieved and that the allowable design limits can be fulfilled.[2] In the European solid breeder blanket concept, both the breeder and neutron multiplier materials are in the form of packed pebble beds. The breeder beds are assemblies of ceramic pebbles highly packed into a metallic structure with helium used as tritium purge gas flowing through the particle assembly. Because of the discrete nature, the macroscopic thermal behavior of the whole bed is the result of the particle-particle, particle-wall, and particle-gas interactions. Furthermore, the breeder bed exhibits strongly coupled thermomechanical behavior.[3] In this framework several parameters such as the packing factor (PF), mechanical state, particle size, gas pressure, and temperature deeply affect the effective properties of the bed, playing a major role in the resultant thermal behavior.[4–22] To characterize the thermomechanical behavior of pebble beds as a result of the particle interactions, the Discrete Element Method (DEM) was confirmed to be a suitable tool[4–12,22,23] guaranteeing to

*E-mail: marigrazia.moscardini@kit.edu

account for the behavior of the material at the microscale level by modeling pebbles individually.

In this work, a DEM approach is used to estimate the temperature profile across the thickness of the breeder bed under fusion-relevant conditions identifying the parameters that mainly affect the thermal behavior of the bed. In particular, the thermal DEM code recently developed at the Karlsruhe Institute of Technology (KIT) to evaluate the effective thermal conductivity of fusion breeder pebble beds was used.[22] According to the Batchelor and O'Brien theory[24] implemented in the code, a network of resistances describes the thermal contacts among particles and between particles and walls accounting for the thermal conduction in the stagnant interstitial gas.[20–22,23] The influence of the gas pressure on the heat conduction in the confined gas region (i.e., Smoluchowski effect[25]) is taken into account.[22] In this study the code described in Ref. 22 was modified to include the neutronic power density as the heat source in the tritium breeder pebbles. In the current work the thermal expansion was not considered; the influence of the mechanical state of the bed is simulated by compressing the assembly in the axial direction. In Sec. II, the implemented discrete element method is presented, and the boundary and loading conditions are described. In Sec. III, the temperature profile generated in the thickness direction of the breeder bed by the neutronic heating is shown, and sensitivity studies are discussed in detail. Finally, the conclusions are reported in Sec. IV.

II. THERMAL MODEL ACCOUNTING FOR THE NEUTRONIC HEATING AS INTERNAL HEAT SOURCE

In this section, the three-dimensional (3-D) thermal network model presented in Ref. 22 is briefly summarized while the changes made to include the neutronic heating as the heat source are described in detail. The simulated geometry with boundary conditions and material properties are then reported.

II.A. Thermal Model

The thermal-DEM code developed at the KIT was employed to investigate the heat transfer in tritium breeder pebble beds of the helium-cooled pebble bed (HCPB)–DEMO blanket. The code, presented in Ref. 22, allows one to evaluate the heat transfer in granular materials accounting for the contribution of the heat conduction through the solid material and the stagnant filling gas. Despite the high temperatures reached in the breeder beds, the contribution of the heat radiation was considered negligible due to both the small particle sizes and high PFs involved.[22] Indeed, according to Refs. 26, 27, and 28, a high PF increases the absorption of heat radiation in a packed structure reducing the radiative bed density,[27] while pebbles with a diameter less than 1 mm show a negligible dependence on thermal radiation in the temperature range of 0 to 1440°C (Ref. 26). According to the Batchelor and O'Brien theory,[24] the implemented 3-D thermal network model simulates the heat transfer in packed systems through chains of resistances describing the thermal contacts between touching particles or particles nearly in contact (particles separated by gaps). Note that since in mechanical DEM the contact forces between spherical particles are calculated from the overlap of their original shapes, touch-type contacts are also called overlap contacts.

Monosized and polydispersed packed granular systems were generated by means of the Random Close Packing (RCP) algorithm described in Refs. 4, 22, and 29. According to the adopted RCP method, a given number of particles with a certain size distribution are packed into a virtual box with a desired thickness. The other two dimensions of the box are determined as a function of the target PF. The target PF is set as the input parameter, and it is evaluated as the ratio between the volume occupied by pebbles over the volume of the box. Because of the small ratio between the thickness of the breeder bed and its radial/toroidal extension, the temperature variation is more significant in the thickness than in the other directions. Therefore, a simplified geometry consisting of an assembly of packed particles in a periodic configuration for the lateral sides and bounded in the upper and the bottom regions by rigid walls was taken as representative in this study. This geometry represents a column cutout of the breeder bed axially bounded by the cooling plates. The temperature profile in the thickness of the breeder bed is evaluated, while in the radial and toroidal directions, the heat exchange is neglected. Therefore, the predicted temperature is expected to be slightly overestimated.

Furthermore, the absence of gravity in the adopted purely geometric RCP method determines a low number of contacts in the generated assemblies.[4,22,29] Therefore, to avoid underestimation of the heat transfer, a slight compression is applied. A precompressive load of 20 kPa was chosen as the minimum value to bring the initial configuration of the investigated assembly closer to real conditions in terms of average number of contacts per particle. With this procedure, the PF increases, according to its definition, with the same percentage as

the axial deformation of the bed. However, at 20 kPa, the variation of the PF is still negligible (about 0.07%) for the investigated assembly.

The compression of the bed, arising in the breeder blanket by the mismatch of the thermal expansion coefficients between pebbles and structural material, is simulated by applying a compressive load. Starting from the configuration generated by the RCP algorithm, the assemblies are progressively loaded up to 6 MPa and then unloaded until the stress in the assembly is lower than 20 kPa. The compression is applied by gradually reducing the height of the upper bounding wall of the bed, while the overall stress in the assembly is obtained as a result of the interaction among particles.[4–8,10,22] According to Refs. 22 and 30, the effective thermal conductivity of the breeder beds is not strongly affected by the compression state. Indeed, because of the relatively low solid-to-gas thermal conductivity ratio, the heat transfer is uniformly distributed between the two phases. Therefore, a variation in terms of compression state and thus in contact area should not deeply affect the thermal behavior of the bed. On the other hand, if different materials are used (e.g., solid materials with high thermal conductivity), the mechanical contacts will certainly play a major role.

After the assembly is generated in such a way, the neutronic heating is applied (details are given below), and the 3-D thermal network model evaluates the heat transfer by thermal resistors defining different types of thermal contacts. At the pebble scale level, the heat flux q_{ij} transferred between two contacting particles i and j is evaluated as

$$q_{ij} = C_{ij}^{eff}\left(T_i - T_j\right) , \tag{1}$$

where

T_i = temperature of particle i

T_j = temperature of particle j

C_{ij}^{eff} = local effective conductance (W/K):

$$C_{ij}^{eff} = \left[\frac{1}{C_i^s} + \frac{1}{C_{ij}^{ct}} + \frac{1}{C_j^s}\right]^{-1} , \tag{2}$$

which is defined by the thermal conductances of the two solid contacting particles C_i^s and C_j^s (W/K) and by the thermal conductance of the thermal contact C_{ij}^{ct} (W/K). As described in Ref. 22, thermal contacts are mainly divided into two types: touching particles or particles separated by gaps. For a detailed description of the individual thermal conductances and the related equations, the reader is referred to Ref. 22. The effective conductance of the thermal contact depends on the particles' size, the size of the gap or contact area, and the thermal conductivities of the solid material k_s (W/m K) and the gas k_g (W/m K). While in the previous work,[22] an axial thermal gradient of 1°C was applied between the top and bottom walls to evaluate the effective thermal conductivity of the granular assembly, in this work a large temperature gradient is expected to be generated by the neutronic heating. Therefore, the temperature-dependent thermal conductivity of both solid material and gas was implemented. In particular, k_s is evaluated for the individual particle as a function of the related temperature assumed in the current time step, while the thermal conductivity of the gas k_g (W/m K) is evaluated for each contact pair at the average temperature of the two particles involved in the thermal contact. In case of touching particles, the thermal conductivity of the contact region has to be defined in the equation of C_{ij}^{ct} reported in Ref. 22.

In this work, the average value between the thermal conductivities of the two particles in contact is applied as thermal conductivity of the contact region. As reported in Ref. 22, the code takes into account the influence of the gas pressure on the gas thermal conductivity. In particular, the thermal conductivity of the gas, thus the effective thermal conductivity of the bed, decreases with its pressure when the gas is confined in small gaps (known as the Smoluchowski effect). The influence of the gas pressure on the gas thermal conductivity, thoroughly explained in Ref. 22 and here briefly summarized to further support the explanations of the results, was realized by introducing the Knudsen number K_n according to the following correlation:

$$k_g^c = \frac{k_g}{1 + 2\beta K_n} , \tag{3}$$

where k_g [W/mK] is the thermal conductivity of the unconfined gas and β represents the amount of energy transfer between the gas molecule and the solid material. It is evaluated as a function of the involved materials according to the equations reported in Ref. 22.

The dependence on the gas pressure p (Pa) is given in the definition of the Knudsen number:

$$K_n = \frac{\mathcal{K}\, T_{ave}}{\sqrt{2}\,\pi d_m^2\, p\, L} , \tag{4}$$

the dependence on the gas pressure p [Pa] is given. Here, $K = 1.38 \cdot 10^{-23}$ [J/K] is the Boltzmann constant, while d_m [m] is the kinetic diameter of the gas molecule.

In order to adapt the implementation of the Smoluchowski effect into a granular material with a large thermal gradient, the Knudsen number is calculated at the average temperature T_{ave} (K) of the two particles in contact. At each time step, q_{ij} (W) is evaluated for each individual contact occurring in the whole assembly. The rate of temperature change $\dot{T}_i$ of the i'th pebble accounting for the neutronic heating reads as

$$\dot{T}_i = \frac{1}{m_i \, c_p} \left(\sum_j q_{ij} + \Psi V_i \right) , \qquad (5)$$

where

m_i = mass of the solid material (kg)

c_p = heat capacity of the solid material (J/kg K)

Ψ = power density due to the neutronic heating (W/m^3)

V_i = volume of the particle i (m^3).

The values of Ψ are reported in Sec. II.B. The thermal diffusion time and condition to end the simulation used in Ref. 22 are applied in this study.

II.B. Boundary Conditions and Thermal Properties

As the starting condition, the temperature of the particles composing the bed as well as the temperature of the upper and bottom walls is set to 500°C. This temperature was selected according to the thermal analysis reported in Refs. 31 and 32. The temperature of the walls is kept constant to simulate the cooling of the bed provided by helium flowing into the cooling plates of the HCPB breeding blanket.[31,32] The temperature of the particles increases according to the applied power density due to the neutronic heating. Figure 1 shows the neutronic power density in the Li_4SiO_4 (considered as bulk material) as a function of the radial distance from the first wall (FW). These data refer to the neutronic calculations presented in Refs. 33 and 34 for an outboard blanket (OB). Unless otherwise stated, the standard conditions refer to assemblies of 5000 spheres of European reference (EU Ref.) material at 95% theoretical density (typical value of the EU Ref. produced pebbles[35]) packed at ~64% with the size distribution reported in Fig. 2. For the helium purge gas, a pressure of 2 bars was chosen as the standard condition according to Refs. 32 and 33, where a reduction from 4 to 2 bars was adopted in favor of a reduction of the tritium permeation into the cooling plates.[36]

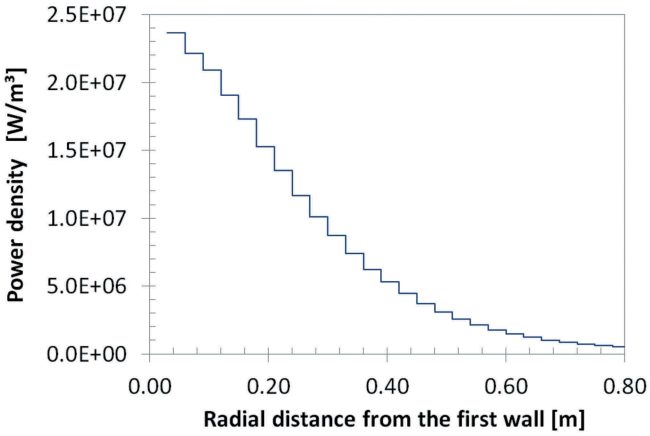

Fig. 1. Neutronic power density for Li_4SiO_4 in OB blanket as a function of the radial distance from the FW (after Refs. 33 and 34).

Since the design of the DEMO HCPB blanket is constantly updated and not yet finalized,[32,33] a bed thickness of 15 mm is here taken as representative and then varied to evaluate its influence on the temperature profile. Because of the simplified geometry adopted in this work and explained in Sec. II.A, a constant power density [Ψ in Eq. (5)] referring to the investigated radial distance from the FW is applied to each pebble in the assembly [multiplying Ψ by the pebble volume V_i as reported in Eq. (5)], while adiabatic conditions are applied at the lateral sides.

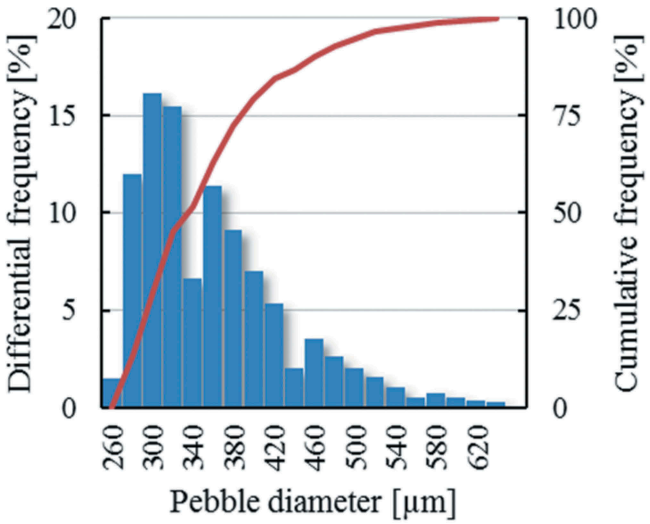

Fig. 2. Size distribution of the EU Ref. material.[30]

To investigate heir influence on the temperature profile of the bed, Li_2TiO_3, Li_2ZrO_3, LiO_2, and Li_4SiO_4 were considered as solid breeder materials. The implemented correlations characterizing the thermal conductivity and heat capacity of the listed solid materials are reported in Table I with the related effective densities and molecular masses. Furthermore, to investigate the influence of different correlations reported in literature and characterizing the thermal conductivity of the same material, a sensitivity study was carried out using the other two correlations reported in Table II for Li_4SiO_4. In Tables I and II "p_r" is the porosity of the solid material.

Since results observed in this section are related to steady-state conditions, which are not influenced by the heat capacity, c_p is kept constant at the value assumed at the starting temperature of 500°C. For the filling gas the implemented thermal properties are reported in Table III.

III. TEMPERATURE PROFILE IN THE BREEDER ZONE

In this section, the temperature profile generated by neutronic heating along the thickness of the breeder bed of the DEMO HCPB blanket is evaluated. Starting from the simplified geometry and relevant conditions for a breeder pebble bed described in Sec. II.A and II.B, different neutronic power densities were applied to resemble different radial positions in the bed. Afterward, parametric sensitivity studies were carried out varying the bed thickness, the filling gas type, the gas pressure, the solid breeder material, and the PF. Then, the effect of the mechanical cyclic loading until the 30th cycle is studied in order to evaluate the influence of the bed compaction on the temperature field of the bed. Finally, the influence of the particles' size is investigated.

III.A. Influence of the Neutronic Power Density

Figure 3 shows the temperature profiles generated across the bed's thickness for an OB HCPB breeding blanket with the conditions described in Sec. II.B. The curves are generated dividing the assembly in 70 layers along the thickness and plotting the average temperature of the particles falling into the same layer at the center plane height of the layer. The different curves refer to different radial distances from the FW. Radial distances from 50 to 450 mm were considered resembling the radial extension of the breeder zone in the HCPB (Refs. 31 and 32). A certain radial distance corresponds to a respective neutronic power density inside the solid breeder material. When the radial distance from the FW increases, the neutronic power density decreases according to the plot in Fig. 1. This generates the highest temperatures in the zone nearest to the FW. Figure 4 exemplarily shows the obtained temperature fields for different radial distances from the FW.

According to the results shown in Figs. 3 and 4, the temperature field strongly changes with the radial position. A peak temperature of about 907°C is reached at the minimum distance of 50 mm considered in this study. This temperature is lower than the design limit of 920°C, which is based on avoiding sintering of pebbles.[47] Increasing the radial distance, the bed temperature strongly decreases, reaching a maximum temperature lower than 580°C at 450 mm from the FW. This affects the tritium residence time (TRT), which is one of the important targets of the breeder blanket. Indeed, the TRT strongly depends on the operating temperature of the breeder beds. Higher temperatures lead to a lower TRT, which is essential to minimizing the tritium inventory inside the breeder zone, avoiding a large tritium release in case of an accident. Therefore, even if the minimum temperature to avoid very low tritium diffusion is around 400°C, higher temperatures (but lower than the design limits) are aimed at guaranteeing the minimum allowable TRT.

III.B. Influence of the Bed Thickness

In the past 10 years, variations of the breeder bed thickness were proposed to optimize the temperature field in the breeder beds assuring an acceptable tritium breeding ratio and tritium extraction and to guarantee the fulfillment of the temperature design limits.[33] In the last proposed design,[32] a thickness of 15.5 mm was adopted. In Ref. 32 the maximum design limit of 920°C to avoid sintering of pebbles was overcome, and a hot spot of 935°C was determined in the breeder material. Starting from the standard conditions reported in Sec. II.B, thicknesses of 10, 15, 15.5, and 20 mm were simulated to investigate the influence of the bed height on the temperature profile. In Fig. 5 the obtained temperature profiles are compared. Results are plotted as a function of the normalized thickness and refer to a radial distance from the FW of ~50 mm. As it has to be expected, because of the longer thermal diffusion path, a larger bed thickness exhibits a higher peak temperature under the same imposed neutronic power density. While using a thickness of 15 mm, the allowable limits are still fulfilled; with a bed of 15.5 mm, the peak temperature reached in the bed is about 924°C. For a thickness of 20 mm, the maximum temperature

TABLE I

Physical Characteristics of the Used Solid Materials

Material	Parameter		Value
EU Ref. (Li_4SiO_4 + 10 mol% Li_2SiO_3)	k_s	(W/m K)	Correlation fitting values in Ref. 37 with the highest density ≈ 89% of theoretical density: $7.317 \times 10^{-12}\ T^4 - 1.302 \times 10^{-8}\ T^3 + 8.712 \times 10^{-6}\ T^2 - 0.002876T + 2.62$; T (°C)
	c_p	(J/kg K)	$\left(-5.33 \times 10^{-7}\ T^2 + 0.001925\ T + 1.238\right) \times 1000$; T (°C) (Ref. 38)
	ρ	(kg/m^3)	$2400(1 - p_r)$; $p_r = 0.05$
	m_s	(g/mol)	119.85
Li_2TiO_3	k_s	(W/m K)	$\left[(1 - p_r)/\left(1 + \left(1.06 - 2.88 \times 10^{-4}\ T\right)p_r\right)\right]\left(4.77 - 5.11 \times 10^{-6}\ T^2\right)$; T (K) (Ref. 39)
	c_p	(J/kg K)	$\left(0.73 + \left(8.44 \times 10^{-4}\ T\right) - \left(1.67 \times 10^{-7}\ T\right)\right) \times 1000$; T (K) (Ref. 39)
	ρ	(kg/m^3)	$3430\ (1 - p_r)$; $p_r \sim 0.08$
	m_s	(g/mol)	109.76
Li_2ZrO_3	k_s	(W/m K)	$(1 - p_r)^{5/3}\left[(3.643/(1 + 0.00155\mathrm{T})) + 7.579 \times 10^{-10}T^3\right]$; T (K) (Ref. 40)
	c_p	(J/kg K)	$\left(1.022 - \left(3.696 \times 10^{-5}\ T\right) - \left(2.791 \times 10^{+4}\ T^{-2}\right) + 8 \times 10^{-5}\ T + 0.0241\right) \times 1000$; T (K) (Ref. 40)
	ρ	(kg/m^3)	$4150(1 - p_r)$; $p_r = 0.2$
	m_s	(g/mol)	153.1
LiO_2	k_s	(W/m K)	$\left[(1 - p_r)^{1.94}\right]\left(0.022 + 1.784 \times 10^{-4}\ T\right)^{-1}$; T (K) (Ref. 41)
	c_p	(J/kg K)	$\left(2.5179 + \left(3.328 \times 10^{-4}\ T\right) - \left(8.382 \times 10^4/T^2\right)\right) \times 1000$; T (K) (Ref. 41)
	ρ	(kg/m^3)	$2013(1 - p_r)$
	m_s	(g/mol)	29.8814

TABLE II

Physical Characteristics of the Li_4SiO_4 Derived from Two Different Studies

Material	Parameter		Value
Li_4SiO_4	k_s	(W/m K)	$2.49\ (1-p_r)^{5/3}\left[\left(1+2.064\times10^{-3}\ T\right)^{-1}+\left(1.85\times10^{-10}\ T^3\right)\right]$; T (K) (Ref. 42)
	c_p	(J/kg K)	$\left(0.890+\left(1.46\times10^{-3}\ T\right)+\left(4.01\times10^{3}\times\ T^{-2}\right)\right)\times1000$; T (K) [(Ref. 42)
Li_4SiO_4	k_s	(W/m K)	$1.98+\left(\frac{850}{T}\right)\times\{(1-p_r)/[1+(p_r\ (2.14-(7\times10^4\times T)))]\}$; T (K) (Ref. 43)
	c_p	(J/kg K)	$939.9+(1.4577\times\ T)-\left(4.011\times10^7/T^2\right)$; T (K) (Ref. 43)

TABLE III

Physical Characteristics of the Used Gas Types

Material	Parameter		Value
Helium	k_g	(W/m K)	$3.366\times10^{-3}\ T^{0.668}$; T (K) (Ref. 44)
	k_d	(m)	2.15×10^{-10} (Ref. 45)
	m_g	(g/mol)	4
Air	k_g	(W/m K)	Correlation fitting values in (Ref. 46): $-1\times10^{-11}\ T^3-\ 4\times10^{-8}\ T^2+8\times10^{-5}\ T+0.0241$; T (°C)
	k_d	(m)	3.66×10^{-10} (Ref. 45)
	m_g	(g/mol)	28.96

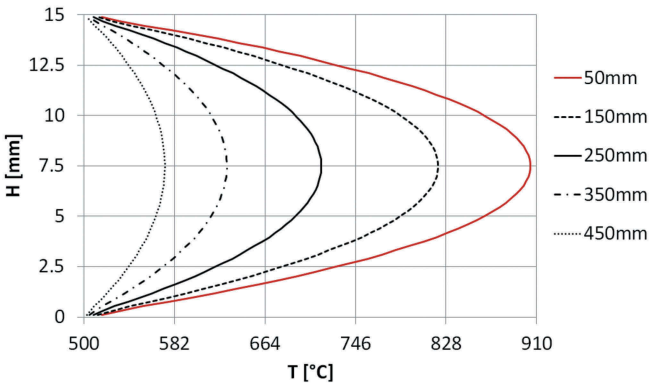

Fig. 3. Temperature profiles generated in the thickness of the breeder material at different radial distances from the FW according to the nuclear heating in Fig. 1.

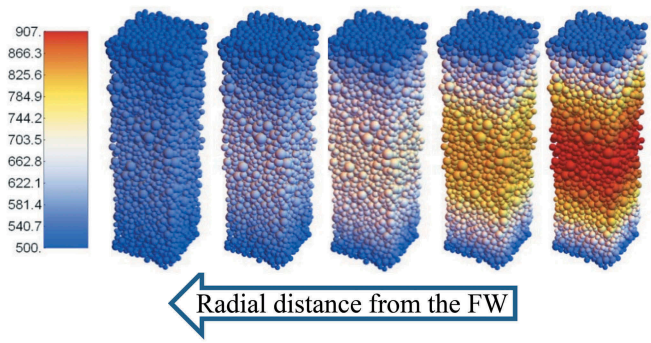

Fig. 4. Temperature field predicted at several distances from the FW (from the left to the right ~450, 350, 250, 150, and 50 mm) according to the nuclear heating in Fig. 1.

overcomes the allowable limit by about 245°C, while in a 10-mm bed, the predicted maximum temperature is about 240°C below the allowable limit for the ceramic breeder material. This suggests that larger bed thicknesses are more suitable for zones with a lower neutronic power density and vice versa. Adjusting the thickness of the bed as a function of the neutronic power density, and thus of the radial distance from the plasma, a higher average temperature could be reached in the whole bed in favor of a lower TRT.

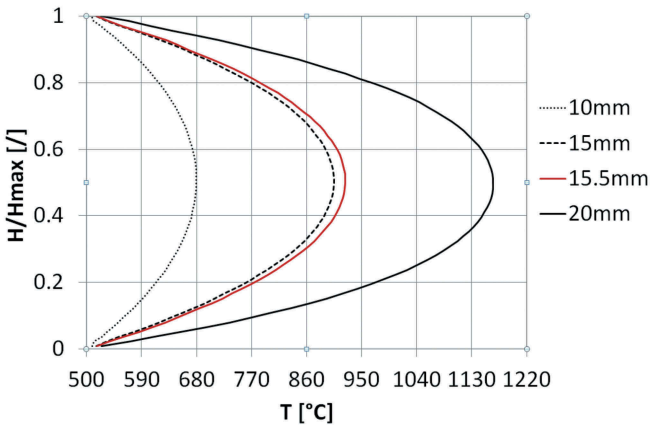

Fig. 5. Temperature profiles generated inside an OB blanket at ~50 mm from the FW for four different bed thicknesses: 10, 15, 15.5, and 20 mm.

III.C. Influence of the Initial PF

Figure 6 shows the temperature profiles generated along the thickness of the breeder bed under standard conditions (see Sec. II.B) at ~50 mm from the FW and for different PFs. Packing factors of about 62.5%, 63%, 64%, and 65% were investigated. Increasing the PF means a proportional increase of the heat deposit per unit pebble bed volume. However, the results show a decrease of the maximum temperature with the increase of the PF. A maximum temperature of 913°C is predicted for a PF of ~62.5%, while the peak temperature decreases to 892°C for a PF of 65%. The reduction of the peak temperature is due to the increase of the total number of thermal contacts (overlaps plus gaps). Figure 7 shows the number of thermal contacts evaluated for the simulated assemblies as the sum of the contacts acting among particles (counted once for each contact pair) and between particles and the top/bottom wall. When the PF increases, the number of the thermal contacts for each particle inside the assembly increases; thus, the number of possible heat flux paths from one particle to its neighbors also increases. This leads to an increase of the effective thermal conductivity of the bed determining a lower temperature. To demonstrate this effect, the code presented in Ref. 22 was used to evaluate the effective thermal conductivity of the investigated assemblies at an average temperature of about 770°C (the average temperature was estimated among the four investigated assemblies). Values of the effective thermal conductivities for the investigated assemblies characterized by different PFs are reported in Table IV. It can be seen that the relative increase of the effective thermal conductivity with the PF is larger than the relative increase of the heat deposit per unit pebble bed volume. Furthermore, Fig. 7 suggests that the increase of the total number of thermal contacts with the PF is mainly due to the increase of the gap-type thermal contacts involved in the heat transfer since the number of the overlaps is almost constant. This is due to the low initial stress level adopted (~20 kPa) for the investigated assemblies. Therefore, for a given amount of particles with the same size distribution packed (according to the procedure described in Sec. II.A) in a defined bed thickness

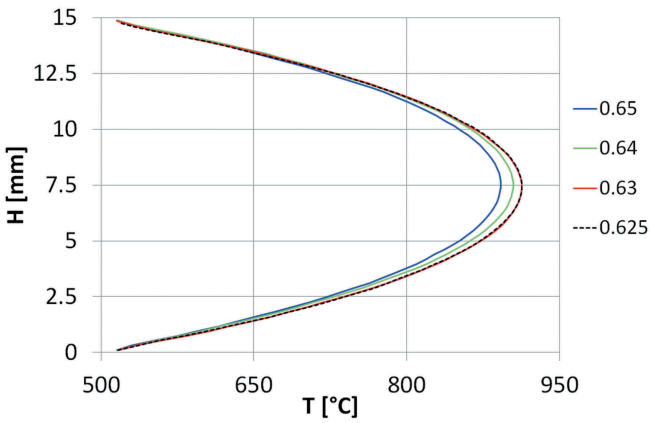

Fig. 6. Temperature profiles obtained with different PFs inside an OB blanket at 50 mm from the FW.

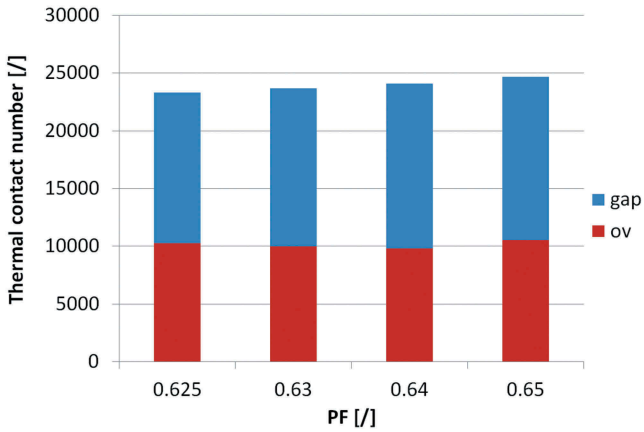

Fig. 7. Number of thermal contacts detected for different PFs.

TABLE IV

Effective Thermal Conductivities of the Investigated Assemblies with Different PFs Evaluated at a Given Average Temperature of 770°C

Packing Factor	0.625	0.63	0.64	0.65
k_{eff} (W/m·K)	1.0005	1.0278	1.0708	1.1239

with a fixed initial stress under a given neutronic power, assemblies exhibit a better heat exchange at higher PFs. This is due to the higher thermal conductivity determined by the larger amount of gap-type thermal contacts involved in the heat transfer.

III.D. Influence of the Gas Pressure and Type

In this section, the influence of the gas pressure as well as of the filling gas type is analyzed. As explained in Sec. II.B, the tritium partial pressure is the driving force behind the tritium permeation into the cooling fluid.[36] Decreasing the purge gas pressure, the tritium permeation is consequently reduced in favor of greater safety. However, even if the reduction of the purge gas pressure is beneficial for the reduction of the tritium permeation into the coolant, it also reduces the effective thermal conductivity of the breeder bed. It was reported that for pressures lower than 1.5 bars, the Smoluchowski effect becomes important.[30,48] For these reasons, in the past years, the pressure of the purge gas was decreased from 4 to 2 bars (Refs. 32 and 33), which is a trade-off between the minimization of the tritium permeation and the maximization of the pressure to avoid the Smoluchowski effect.

Figure 8 shows the influence of the helium pressure at 4, 2, 1, and 0.1 bars on the temperature profiles generated for the same assembly under standard conditions (see Sec. II.B). As expected, an increase of the temperature is obtained when the gas pressure decreases. While slight increases of about 1.7% and 5% occur in terms of the peak temperatures when the gas pressure is reduced from 4 to 2 bars and 1 bar, respectively, the peak temperature increases by about 52% when the gas pressure decreases down to 0.1 bar. At 1 and 0.1 bar the temperature limit of 920°C is overcome reaching maximum temperatures of 933°C and 1350°C, respectively. This behavior is due to the Smoluchowski effect, which determines a reduction of the thermal conductivity of the confined gas with the pressure. This leads to a reduction of the conductance in the thermal contacts; thus, a lower heat flux is exchanged between particles.

Figure 9 shows the probability distributions of the effective thermal conductances C_{ij}^{eff} evaluated at 4, 2, 1, and 0.1 bars for the analyzed assembly. To evaluate the probability distribution reported in Fig. 9, the thermal contacts among particles and between particles and the top/bottom wall were considered. As anticipated, the mean value of C_{ij}^{eff} is shifted to lower values when the gas pressure decreases.

Considering an accident scenario such as an ex-vessel loss-of-coolant accident determined by the failure of the main helium pipes forming the first confinement barrier,[49] the subsequent evolution of the accident could lead to the entrance of air into the breeder zone. In Fig. 10 the temperature profiles generated inside the breeder bed under standard conditions (see Sec. II.B) at 50 mm from the FW are reproduced changing the filling gas from helium to air. Furthermore, the influence of the gas pressure at 2 bars and 1 bar is analyzed for both gases. Comparing the results obtained at a given gas pressure, an increase of ~30% to 40% is observed in terms of peak temperature when the filling gas is changed from helium to air. This is due to the different thermal conductivities of the two gases. Indeed, the thermal conductivity of air is about 40% lower than the helium thermal conductivity. Figure 11 shows the probability distributions of the

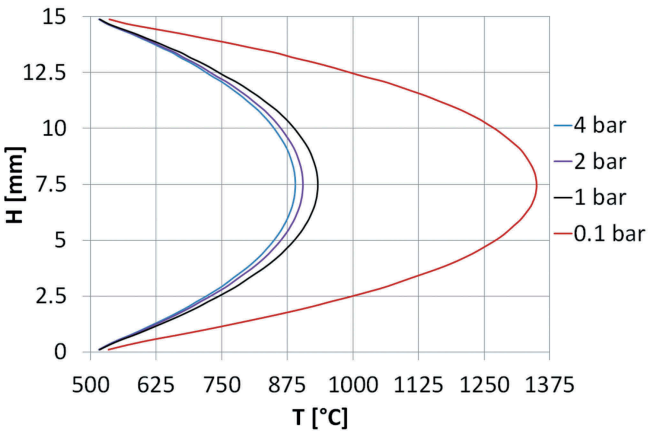

Fig. 8. Temperature profiles inside an OB blanket at 50 mm for the FW for different helium pressures.

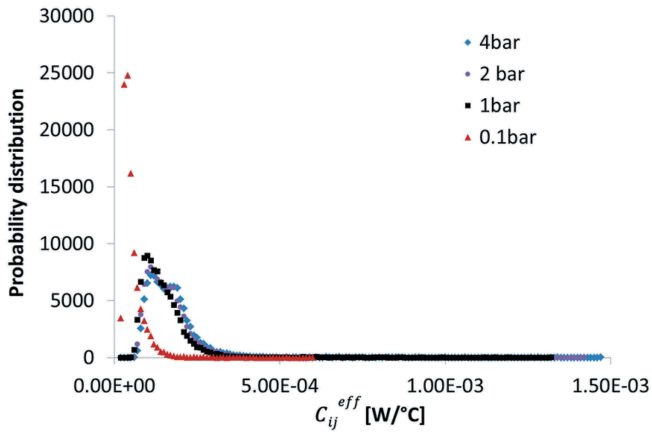

Fig. 9. Probability distributions of the effective thermal conductances C_{ij}^{eff} evaluated at 4, 2, 1, and 0.1 bars for the same polydispersed assembly.

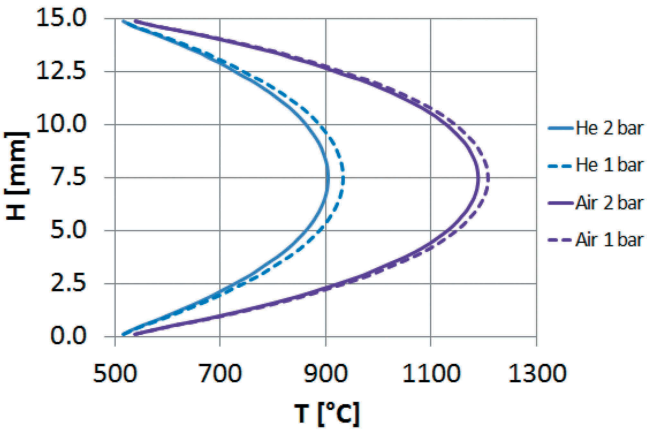

Fig. 10. Temperature profiles generated at 50 mm from the FW with helium and air used as filling gas, both at 2 bars and 1 bar.

effective thermal conductances evaluated for thermal contacts considering only gap-type thermal contacts. Since air has a lower thermal conductivity, for a fixed particle configuration and at a given pressure, the peak of the distribution is shifted to lower values compared to helium. Furthermore, it has to be noticed that decreasing the pressure from 2 bars to 1 bar, the peak temperature in air is increased by about 1.6% versus by about 3% in helium. This reflects the different reduction of the gas thermal conductivity with pressure, as will be explained now.

In Fig. 12, the S-shaped curves representing the reduction of the gas thermal conductivity with the gas pressure are reported for helium and air at 500°C. The curves are obtained by means of Eqs. (3) and (4) for a fixed gap size of 30 μm and the gas properties reported in Table III. Both gas thermal conductivities shown in Fig. 12 are normalized to the respective gas thermal conductivity at an unconfined condition. In air, the onset of the transition region is shifted to lower pressures resulting in a larger continuum region. This determines a lower slope of the curve between 1 and 2 bars in air than in helium. In particular, in the pressure range 1 to 2 bars, the helium thermal conductivity decreases by about 40%, while a reduction of ~3% is observed in air.

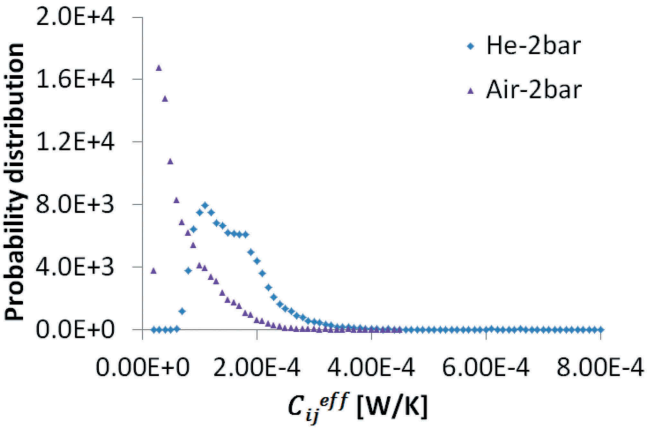

Fig. 11. Probability distributions of the effective thermal conductances C_{ij}^{eff} evaluated using helium and air at 2 bars as filling gas.

III.E. Influence of the Solid Material

In order to study the influence of the solid material, three different investigations have been carried out. First, sensitivity studies were performed varying the thermal conductivity of the solid material. Then, the temperature profiles generated using different tritium breeder materials were compared, and the influence of the porosity was investigated. Finally, the influence of different correlations reported in literature characterizing the thermal conductivity of the same solid material was analyzed. The simulations were carried out with the conditions defined as "standard" in Sec. II.B. The results were obtained with the same assembly generated according to the procedure described in Sec. II.A. The applied neutronic power density was evaluated at 50 mm from the FW.

For the first investigation, the thermal conductivity of the EU Ref. material was first varied by ±5% according to the uncertainty reported in Ref. 37 to evaluate the influence of the experimental error on the simulated thermal behavior of the bed. Then, the thermal conductivity was varied by ±10% to investigate the maximum acceptable deviation for the fulfillment of the temperature design limits. The results are summarized in Fig. 13 (dashed and dotted lines) and

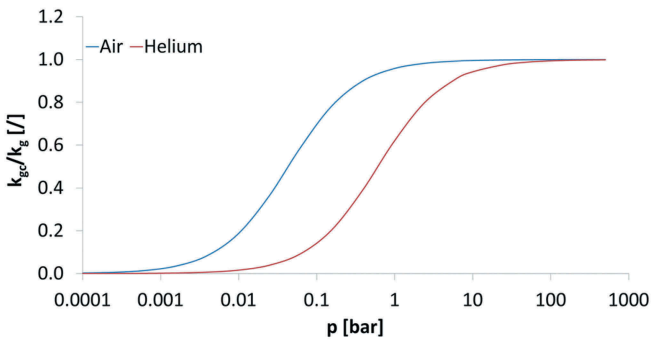

Fig. 12. S-shaped curves obtained for helium and air at 500°C for a fixed gap size of 30 μm by means of Eqs. (3) and (4) applying values reported in Table III.

compared to the temperature profile obtained with the reference thermal conductivity (solid black line). The results confirm that a decrease of the solid thermal conductivity leads to an increase of the temperature in the bed and vice versa. In particular, a variation of ±1.3% and ±3% in terms of peak temperature was predicted when the thermal conductivity is changed by ±5% and ±10%, respectively. While a reduction of 5% determines a peak temperature of about 917°C, thus still fulfilling the temperature limit of 920°C, a reduction of 10% generates an unacceptable maximum temperature of 931°C in the simulated conditions. Increasing the thermal conductivity by about 5% to 10%, the peak temperature slightly decreases without compromising the TRT as explained in Sec. III.A.

As a second step, the temperature profiles obtained using EU Ref., Li_2ZrO_3, LiO_2, and Li_2TiO_3 as solid materials with the same porosity (11%) have been evaluated. Since the solid materials exhibit different thermal conductivities under different porosities,[37,39,40] the influence of the porosity was investigated, additionally, since the porosity of the currently produced pebbles ranges from ~5% (Ref. 35) to ~13% (Ref. 50). This sensitivity study was carried out for Li_2TiO_3 reducing the porosity from 11% to 5%. The results are shown in Fig. 14. The solid lines refer to different solid materials with the same porosity of 11%, while the dashed line indicates the temperature profile of Li_2TiO_3 pebbles at 5% porosity. The results demonstrate that materials with a higher thermal conductivity than LiO_2 more easily transfer the heat generated by the neutronic heating reaching a lower temperature for the given thickness. According to the thermal conductivities evaluated with the correlation reported in Table I, a slight deviation occurs between results obtained using Li_2TiO_3 and EU Ref. materials. Comparing

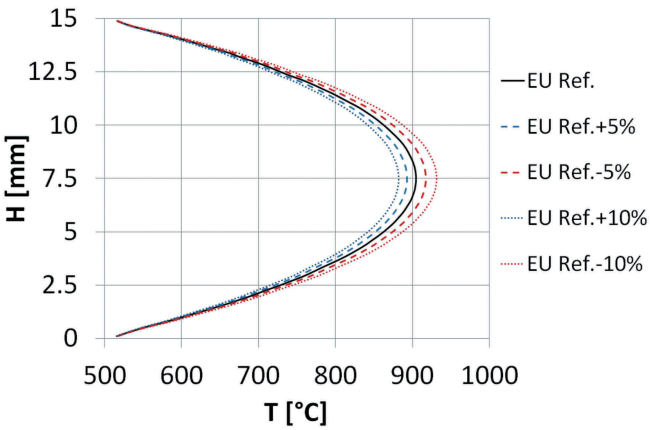

Fig. 13. Temperature profiles generated at 50 mm from the FW varying the thermal conductivity of the EU Ref. material.

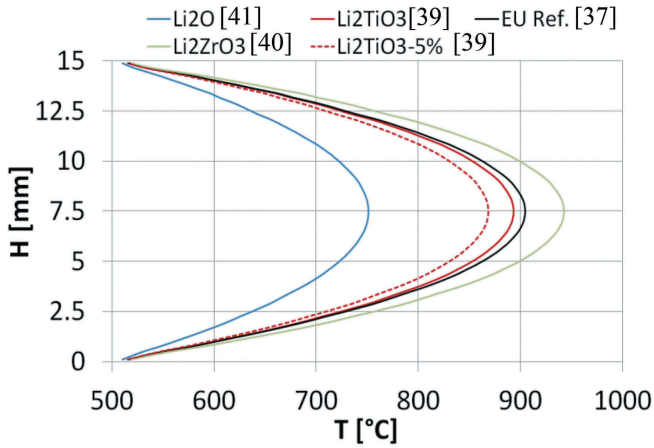

Fig. 14. Temperature profiles generated at 50 mm from the FW using the EU Ref., Li_2ZrO_3, LiO_2, and Li_2TiO_3 as solid materials.

the solid and dashed red curves, the influence of the porosity can be estimated for Li_2TiO_3. The porosity-dependent thermal conductivity was calculated with the correlation reported in Ref. 39. Because of the reduction of the voids, when the porosity decreases, the thermal conductivity of the solid material increases, determining a lower temperature in the assembly. In this specific case, a reduction of 6% in porosity leads to a reduction of about 2.6% in terms of peak temperature.

Finally, the influence of the implemented correlation used to evaluate the thermal conductivity of a solid material has been investigated. In Fig. 15, three temperature profiles are shown. The three curves are generated using three different correlations to evaluate the thermal conductivity of Li_4SiO_4 at 11% of porosity according to the formulas reported in Tables I and II. While a negligible difference occurs using the correlations reported in Refs. 37 and 43, the temperature profile using the correlation given in Ref. 42 greatly differs. Because of the much lower thermal conductivity evaluated in Ref. 42, the peak temperature is well above the temperature limit for Li_4SiO_4, and the major part of the bed thickness experiences temperatures above 920°C.

III.F. Influence of the Cycling Load

In order to investigate the influence of the compression level and particle rearrangement on the heat transfer in the breeder pebble beds, a cyclic load was applied on the standard assembly (see Sec. II.B). Figure 16 shows the stress-strain curves resulting from the 1st, 2nd, 5th, 10th, and 30th cycles, which were considered for the analysis reported in this section. The assembly is cyclically loaded until 6 MPa and unloaded down to ~20 kPa. In Fig. 17 the

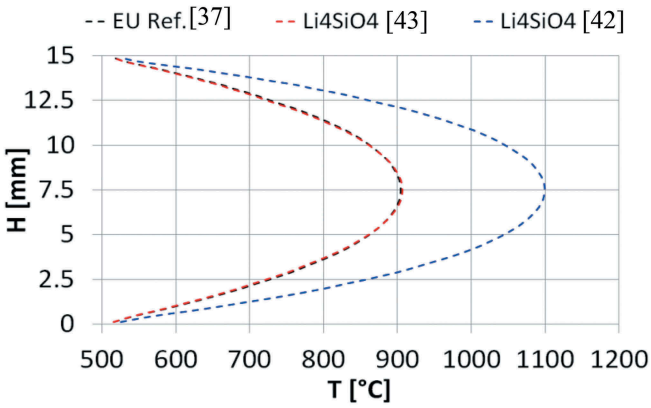

Fig. 15. Temperature profiles generated at 50 mm for three different correlations reported in literature for the thermal conductivity of the Li_4SiO_4 at 11% of porosity.

temperature profiles at 50 mm from the FW at ~20 kPa and ~6 MPa for the listed cycle number are shown.

For a given stress level, the results exhibit a negligible variation of the temperature profile with cycling. In terms of peak temperature, a reduction of about 0.5% is detected after 30 cycles. For the given cycle the peak temperature decreases by about 1% when the assembly is compressed from about 20 kPa to 6 MPa. In Figs. 18 and 19, the variations of the total effective thermal conductances and of the total contact number, given by overlap-type contacts (red zone) and gap-type thermal contacts (blue zone), are shown as a function of the compression state for the corresponding cyclic load, respectively.

Here, the total effective thermal conductance is defined as the sum of all thermal conductances of the thermal contacts detected: first, among particles in the

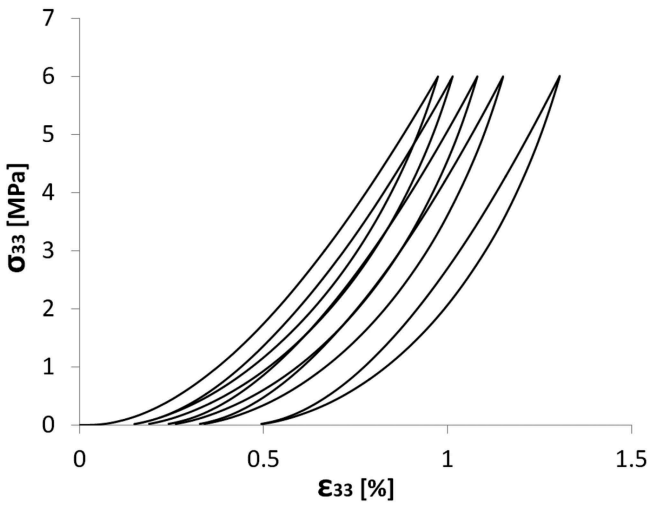

Fig. 16. Stress-strain curves resulting from the 1st, 2nd, 5th, 10th, and 30th load cycles.

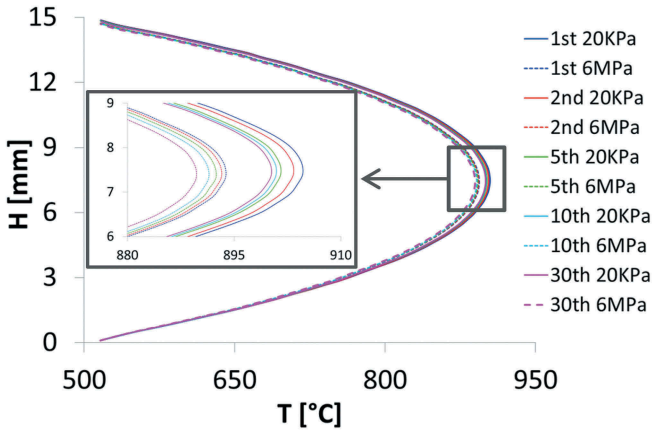

Fig. 17. Temperature profiles generated at 50 mm from the FW at the compression state of the corresponding cyclic point reported in the legend.

assembly and second, with the top and bottom walls. Peaks and valleys alternate when the assembly is loaded and unloaded, respectively. By loading the assembly, new contacts are generated when small gaps turn into overlaps and the existing contact areas increase. This leads to an increase of the total thermal conductance given by overlaps associated with a reduction of the gap total thermal conductance. The opposite occurs when the assembly is unloaded. Furthermore, after each unloading some particles take different equilibrium positions as in previous cycles leading to a higher number of contacts and thus a higher $C^{eff}_{sum\_ov}$. This leads to an increase of the total heat flux exchanged among particles generating the slight reduction of the temperature field shown in Fig. 17.

III.G. Influence of the Particle Size

In this section, the influence of the particle size on the heat transfer in the breeder pebble bed is investigated. Temperature profiles generated across the bed thickness with assemblies of monosized and polydispersed particles are compared to each other. In Fig. 20 four temperature profiles obtained under standard conditions (see Sec. II.B) referring to a polydispersed (see Fig. 2) packed bed and three assemblies of monosized particles with different radii of 0.13, 0.22, and 0.32 mm are shown. The three chosen radii refer to the maximum, minimum, and average values of the size distribution given in Fig. 2. When the radius of the particles increases, the peak temperature reached inside the bed decreases. This occurs because larger contact areas are involved in assemblies composed of bigger spheres. As shown in Fig. 21, when the radius of the particles increases, the mean contact radius is shifted to higher values.

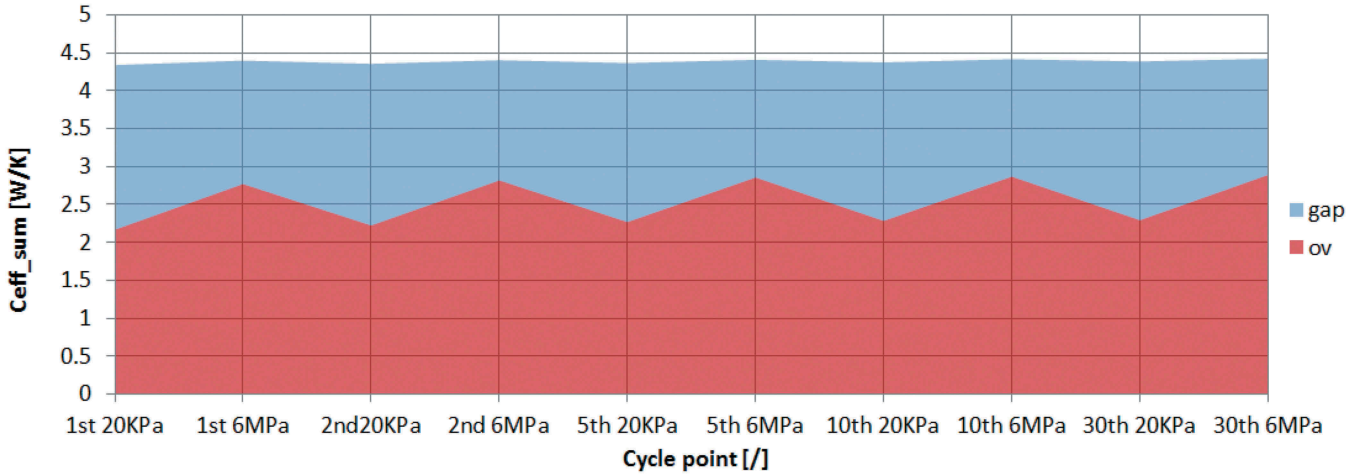

Fig. 18. Total effective thermal conductances C_{sum}^{eff} of gaps and overlaps evaluated at the compression state of the corresponding cyclic load reported in the legend.

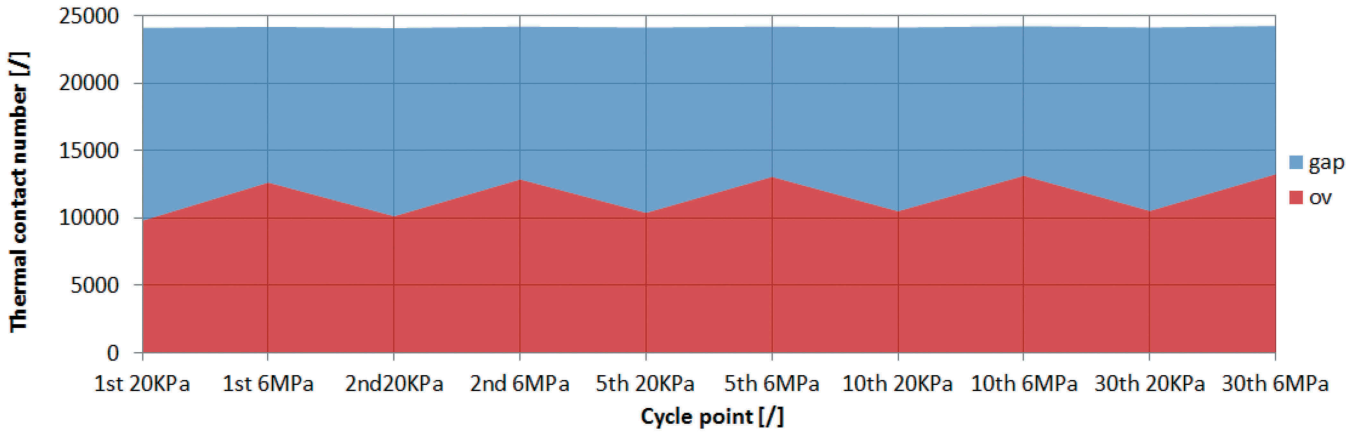

Fig. 19. Thermal contact number of gaps and overlaps evaluated at the compression state of the corresponding cyclic load reported in the legend.

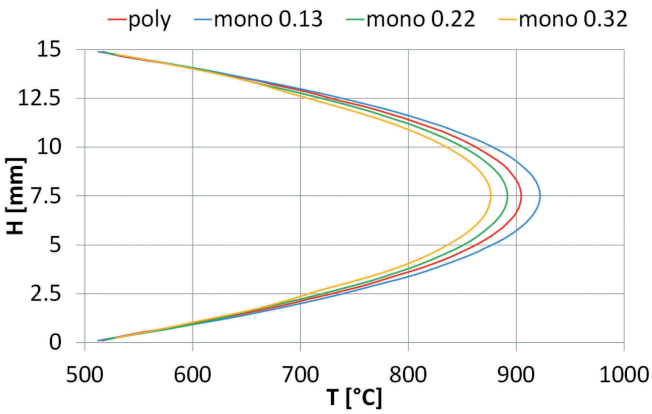

Fig. 20. Temperature profiles at 50 mm from the FW with assemblies of polydispersed (see Fig. 2) and monosized particles with different radii.

Larger contact areas determine a higher effective thermal conductivity of the bed leading to a lower temperature field in the bed. For the same reason, since the mean value of the radius of the applied polydispersed size distribution is about 0.15 to 0.16 mm, the temperature profile of the polydispersed assembly falls between curves of the monosized packed particle with radii of 0.13 and 0.22 mm. Therefore, under the simulated conditions, if the peak of the size distribution of the currently produced pebbles (Fig. 2) is shifted to a lower size, it has to be expected that there is a slight increase of the maximum temperature generated in the bed that is beyond the design limits. In Fig. 22 the total effective thermal conductances for the corresponding heat transfer modes are reported as a function of the particle size for both overlaps and gaps.

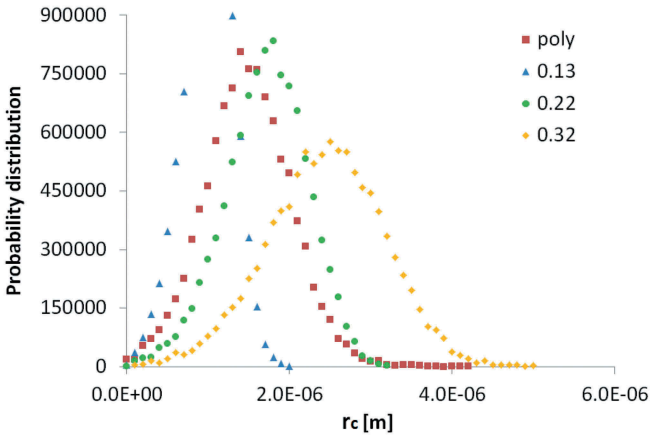

Fig. 21. Probability distribution of contact radii. Different curves refer to assemblies of polydispersed (see Fig. 2) and monosized particles with different radii.

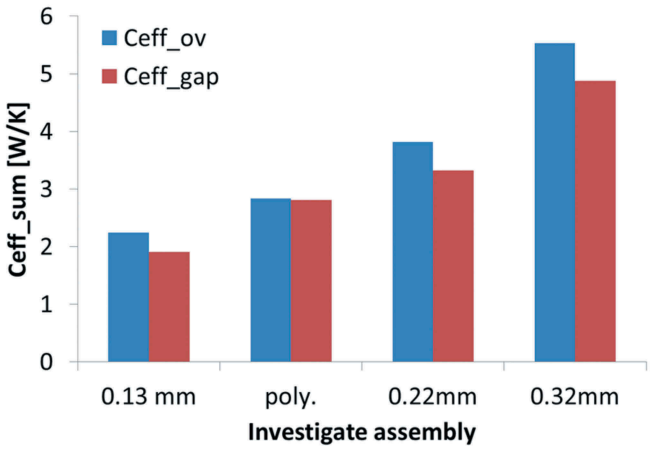

Fig. 22. Total effective thermal conductances C_{sum}^{eff} of gaps and overlaps as a function of the particle size.

Both quantities increase with the particle size, showing an almost even distribution of the heat transfer between overlaps and gaps within the studied size range. This is due to the relatively low solid-to-gas thermal conductivity ratio that characterizes the breeder beds. Larger particles involve larger gaps increasing the gas thermal conductivity according to the reduction of the Smoluchowski effect.[22] This once more confirms the importance of the Smoluchowski effect in granular ceramic breeder beds. The results also show an increase of the heat transfer attributing to the larger contact area involved.

IV. CONCLUSIONS

In the framework of the research studies for the design of the solid breeder blanket concept, DEM analyses are essential to predict the behavior of fusion pebble beds as a result of the interactions occurring in the bed at the pebble scale. In this work, the recently developed in-house thermal DEM code was applied to study the heat transfer inside ceramic breeder pebble beds evaluating the temperature profiles generated by neutronic heating in the thickness of the breeder zone of the DEMO HCPB blanket. A column cutout of the breeder bed bounded by upper and bottom walls resembling the cooling plates was simulated. The effects of relevant blanket parameters such as PF, pebble material and size, characteristics of the purge gas, compressive load, and bed height were investigated. Since the code accounts for the Smoluchowski effect, the effect of the gas pressure on the temperature profile in the thickness of the breeder bed was estimated.

A strong influence of the neutronic heating acting along the radial length of the breeder zone was established. Increasing the radial distance from the plasma face, the neutronic heating decreases, determining a lower bed temperature for a given thickness. In particular, for a bed thickness of 15 mm, peak temperatures of about 907°C and 573°C were detected at 50 and 450 mm from the FW, respectively. Under the simulated conditions, the predicted values satisfy the temperature limit of 920°C, avoiding the sintering of pebbles. Sensitivity studies of the bed thicknesses showed that higher beds generate higher temperatures under the same imposed power density due to the longer heat transfer path. While at 50 mm, beds higher than 15 mm should be avoided to fulfill the temperature limit, thicker beds are admissible for zones with a lower power density to further decrease the TRT. As a further sensitivity study, the influence of the gas pressure was investigated. Reducing the gas pressure from 2 bars to 1 bar, an increase of the peak temperature by 5% is detected, and the limit of 920°C is already overcome under the simulated conditions. Falling in the midst of the transition region in the Smoluchowski effect of He, pressures lower than 1 bar drastically reduce the effective thermal conductivity of the bed generating temperatures even higher than 1000°C. Moreover, this work revealed the importance of the size distribution of the produced pebbles in the heat transfer process. In particular, when the peak of the size distribution is shifted to lower diameters, a higher maximum temperature is reached in the bed. A variation of 40% of the pebbles' diameter determines a variation of about 3.4% of the peak temperature in the bed. Finally, the influence of the solid material was evaluated, and the effect of the porosity was estimated. According to the obtained results, when the porosity increases, the thermal conductivity of the solid material decreases, generating

a lower temperature field in the bed. At the same time, our studies revealed the necessity to create a reliable database characterizing the thermal properties of the solid materials with valid correlations.

References

1. S. KONISHI et al., "Functional Materials for Breeding Blankets—Status and Developments," *Nucl. Fusion*, **57**, 092014 (2017); https://doi.org/10.1088/1741-4326/aa7e4e.
2. "Tritium Breeding," ITER Machine website; https://www.iter.org/mach/TritiumBreeding (current as of July 12, 2018).
3. Z. LU et al., "Numerical and Experimental Prediction of the Thermomechanical Performance of Pebble Beds for Solid Breeder Blanket," *Fusion Eng. Des.*, **49-50**, 605 (2000); https://doi.org/10.1016/S0920-3796(00)00348-3.
4. Y. GAN and M. KAMLAH, "Discrete Element Modelling of Pebble Beds: With Application to Uniaxial Compression Tests of Ceramic Breeder Pebble Beds," *J. Mech. Phys. Solids*, **58**, 129 (2010); https://doi.org/10.1016/j.jmps.2009.10.009.
5. R. K. ANNABATTULA, Y. GAN, and M. KAMLAH, "Mechanics of Binary and Polydisperse Spherical Pebble Assembly," *Fusion Eng. Des.*, **87**, 853 (2012); https://doi.org/10.1016/j.fusengdes.2012.02.033.
6. S. ZHAO et al., "Failure Initiation and Propagation of Li_4SiO_4 Pebbles in Fusion Blankets," *Fusion Eng. Des.*, **88**, 8 (2013); https://doi.org/10.1016/j.fusengdes.2012.09.008.
7. S. PUPESCHI et al., "Numerical and Experimental Characterization of Ceramic Pebble Beds Under Cycling Mechanical Loading," *Fusion Eng. Des.*, **112**, 162 (2016); https://doi.org/10.1016/j.fusengdes.2016.08.021.
8. S. PUPESCHI et al., "Cyclic Behavior of Ceramic Pebble Beds Under Mechanical Loading," *Fusion Eng. Des.*, **134**, 11 (2018); https://doi.org/10.1016/j.fusengdes.2018.06.009.
9. Z. AN et al., "Application of Discrete Element Method to Study Mechanical Behaviors of Ceramic Breeder Pebble Beds," *Fusion Eng. Des.*, **82**, 2233 (2007); https://doi.org/10.1016/j.fusengdes.2007.02.004.
10. M. MOSCARDINI et al., "A Discrete Element Method to Simulate the Mechanical Behavior of Ellipsoidal Particles for a Fusion Breeding Blanket," *Fusion Eng. Des.*, **12**, 22 (2017); https://doi.org/10.1016/j.fusengdes.2017.05.110.
11. J. T. VAN LEW et al., "A Discrete Element Method Study on the Evolution of Thermomechanics of a Pebble Bed Experiencing Pebble Failure," *Fusion Eng. Des.*, **89**, 1151 (2014); https://doi.org/10.1016/j.fusengdes.2014.04.066.
12. H. ZHANG et al., "Investigation on the Packing Behaviors and Mechanics of Li4SiO4 Pebble Beds by Discrete Element Method," *Fusion Eng. Des.*, **125**, 551 (2017); https://doi.org/10.1016/j.fusengdes.2017.04.049.
13. A. ABOU-SENA et al., "Effective Thermal Conductivity of Lithium Ceramic Pebble Beds for Fusion Blankets: A Review," *Fusion Sci. Technol.*, **47**, 1094 (2005); https://doi.org/10.13182/FST05-3.
14. J. EARNSHAW et al., "The Effective Thermal Conductivity of Bed of 1.2-mm-diam Lithium Zirconate Spheres in Helium," *Fusion Technol.*, **33**, 31 (1998); https://doi.org/10.13182/FST98-A13.
15. T. HATANO et al., "Effective Thermal Conductivity of a Li_2TiO_3 Pebble Bed for a Demo Blanket," *Fusion Sci. Technol.*, **44**, 94 (2003); https://doi.org/10.13182/FST03-A316.
16. A. ABOU-SENA et al., "Experimental Measurements of the Effective Thermal Conductivity of a Lithium Titanate (Li_2TiO_3) Pebbles-Packed Bed," *J. Mater. Process. Tech.*, **181**, 206 (2007); https://doi.org/10.1016/j.jmatprotec.2006.03.061.
17. M. PANCHAL et al., "Numerical Modelling for the Effective Thermal Conductivity of Lithium Metatitanate Pebble Bed with Different Packing Structures," *Fusion Eng. Des.*, **112**, 303 (2016); https://doi.org/10.1016/j.fusengdes.2016.08.027.
18. M. ENOEDA et al., "Measurement of Effective Thermal Conductivity of Lithium Oxide and Beryllium Packed Bed," *Proc. 15th IEEE/NPSS Symp. Fusion Engineering*, Hyannis, Massachusetts, October 11–15, 1993, p. 282, Institute of Electrical and Electronics Engineers/Nuclear and Plasma Sciences Society (1994).
19. N. ZACCARI and D. AQUARO, "Mechanical Characterization of Li_2TiO_3 and Li_4SiO_4 Pebble Beds: Experimental Determination of the Material Properties and of the Pebble Bed Effective Value," *Fusion Eng. Des.*, **82**, 2375 (2007); https://doi.org/10.1016/j.fusengdes.2007.05.008.
20. T. S. YUN and T. M. EVANS, "Three-Dimensional Random Network Model for Thermal Conductivity in Particulate Materials," *Comput. Geotech.*, **37**, 991 (2010); https://doi.org/10.1016/j.compgeo.2010.08.007.
21. S. KANUPARTHI et al., "An Efficient Network Model for Determining the Effective Thermal Conductivity of Particulate Thermal Interface Materials," *IEEE Trans. Compon. Packag. Technol.*, **31**, 611 (2008); https://doi.org/10.1109/TCAPT.2008.2001839.
22. M. MOSCARDINI et al., "Discrete Element Method for Effective Thermal Conductivity of Packed Pebbles Accounting for the Smoluchowski Effect," *Fusion Eng. Des.*, **127**, 192 (2018); https://doi.org/10.1016/j.fusengdes.2018.01.013.
23. Y. GAN et al., "Thermal Discrete Element Analysis of EU Solid Breeder Blanket Subjected to Neutron Irradiation," *Fusion Sci. Technol.*, **66**, 83 (2014); https://doi.org/10.13182/FST13-727.
24. G. K. BATCHELOR and R. W. O'BRIEN, "Thermal or Electrical Conduction Through a Granular Material," *Proc. R. Soc. London A*, **355**, 313 (1977); https://doi.org/10.1098/rspa.1977.0100.

25. M. SMOLUCHOWSKI, "Über den Temperatursprung bei Wärmeleitung in Gasen," *Pisma Mariana Smoluchowskiego*, **1**, *1*, 113 (1924).

26. Y. ASAKUMA et al., "Thermal Radiation Analysis of Packed Bed by a Homogenization Method," *Int. J. Heat Mass Transfer*, **73**, 97 (2014); https://doi.org/10.1016/j.ijheatmasstransfer.2014.01.065.

27. X. LU et al., "Correlation Between Structure and Thermal Conductivity of Organic Aerogels," *J. Non-Cryst. Solids*, **1995**, 226 (2016); https://doi.org/10.1016/0022-3093(95)00191-3.

28. H. WU et al., "Effect of Scale on the Modeling of Radiation Heat Transfer in Packed Pebble Beds," *Int. J. Heat Mass Transfer*, **101**, 562 (2016); https://doi.org/10.1016/j.ijheatmasstransfer.2016.05.090.

29. Y. GAN et al., "Computer Simulation of Packing Structure in Pebble Beds," *Fusion Eng. Des.*, **85**, 1782 (2010); https://doi.org/10.1016/j.fusengdes.2010.05.042.

30. S. PUPESCHI et al., "Effective Thermal Conductivity of Advanced Ceramic Breeder Pebble Beds," *Fusion Eng. Des.*, **116**, 73 (2017); https://doi.org/10.1016/j.fusengdes.2017.01.026.

31. F. HERNÁNDEZ et al., "Fluid Dynamics and Thermal Analysis of a HCPB TBM Breeder Unit Mock-Up," *Fusion Eng. Des.*, **86**, 2278 (2011); https://doi.org/10.1016/j.fusengdes.2011.04.053.

32. F. HERNANDEZ et al., "A New HCPB Breeding Blanket for the EU DEMO: Evolution, Rationale and Preliminary Performances," *Fusion Eng. Des.*, **124**, 882 (2017); https://doi.org/10.1016/j.fusengdes.2017.02.008.

33. F. HERNÁNDEZ et al., "HCPB Design Report 2015," ID BB-1.2.1-T002-D001, EUROfusion (2016).

34. P. PERESLAVTSEV et al., "Neutronic Analyses for the Optimization of the Advanced HCPB Breeder Blanket Design for DEMO," *Fusion Eng. Des.*, **124**, 910 (2017); https://doi.org/10.1016/j.fusengdes.2017.01.028.

35. T. SHIKAMA et al., "Status of Development of Functional Materials with Perspective on Beyond-ITER," *Fusion Eng. Des.*, **83**, 976 (2008); https://doi.org/10.1016/j.fusengdes.2008.07.034.

36. D. R. HANCHAR and M. S. KAZIM, "A Tritium Permeation Model for Conceptual Fusion Reactor Designs," *J. Fusion Energy*, **3**, 47 (1983); https://doi.org/10.1007/BF01053467.

37. B. LÖBBECKE et al., "Thermal Conductivity of Sintered Lithium Orthosilicate Compacts," *J. Nucl. Mater.*, **386–388**, 1068 (2009); https://doi.org/10.1016/j.jnucmat.2008.12.281.

38. R. KNITTER, Internal Communication, Karlsruhe Institute of Technology (2017).

39. S. SAITO et al., "Density Dependence on Thermal Properties of Li2TiO3 Pellets," *J. Nucl. Mater.*, **253**, 213 (1998); https://doi.org/10.1016/S0022-3115(97)00314-0.

40. P. GIERSZEWSKI, "Thermal Conductivity of Lithium Metazirconate," *Fusion Technol.*, **23**, 333 (1993); https://doi.org/10.13182/FST93-A30162.

41. O. KRIKORIAN, "Estimation of the Thermophysical and Mechanical Properties and the Equation of State of Li_2O," *High Temp-High Press.*, **17**, 161 (1985).

42. M. BILLONE et al., "ITER Solid Breeder Blanket Materials Database," Argonne National Laboratory (1993).

43. "Thermal and Structural Properties of Fusion Related Materials, LITHIUM SILICATE (Li_4SiO_4)," ARIES Program, Public Information Site; http://www-ferp.ucsd.edu/LIB/PROPS/PANOS/li4sio4.html (current as of July 12, 2018).

44. A. ABOU-SENA and A. YING, "Effective Thermal Conductivity of Lithium Ceramic Pebble Beds for Fusion Blankets: A Review," *Fusion Sci. Technol.*, **47**, 1094 (2005); https://doi.org/10.13182/FST05-3.

45. D. R. LIDE, *CRC Handbook of Chemistry and Physics*, 95th ed., CRC Press (2004).

46. The Engineering ToolBox website; http://www.engineeringtoolbox.com (current as of July 12, 2018).

47. F. HERNÁNDEZ et al., "Thermo-Mechanical Analyses and Assessment with Respect to the Design Codes and Standards of the HCPB-TBM Breeder Unit," *Fusion Eng. Des.*, **87**, 1111 (2012); https://doi.org/10.1016/j.fusengdes.2012.02.088.

48. S. YAGI and D. KUNII, "Studies on Heat Transfer near Wall Surface in Packed Beds," *AiChE J.*, 97 (1960); https://doi.org/10.1002/aic.690060119.

49. L. V. BOCCACCINI et al., "Review of Safety Issues for the European HCPB Test Blanket System," *Nucl. Fusion*, **47**, S436 (2007); https://doi.org/10.1088/0029-5515/47/7/S04.

50. T. HOSHINO, "Development of Fabrication Technologies for Advanced Tritium Breeder Pebbles by the Sol-Gel Method," *Fusion Eng. Des.*, **88**, 2264 (2013); https://doi.org/10.1016/j.fusengdes.2013.05.025.